# Solar Soft/Hard X-ray Photometer–Imager aboard the INTERBALL-Tail Probe

J. Sylwester*
*Space Research Centre, Polish Academy of Sciences, 51-622, Kopernika 11, Wrocław*

F. Fárník
*Astronomical Institute, Academy of Sciences of the Czech Republic, 251 65 Ondrejov*

O. Likin
*Space Research Institute, Russian Academy of Sciences, Profsoyuznaya St. 84/32, Moscow*

Z. Kordylewski, M. Siarkowski, S. Nowak, S. Płocieniak, W. Trzebiński
*Space Research Centre, Polish Academy of Sciences, 51-622, Kopernika 11, Wrocław*

**Abstract.** We describe the RF15-I instrument, comprising a solar photometer and an imager, designed for multiband high time resolution measurements of integral solar fluxes in the energy range between 2 keV and 240 keV as well as for imaging of solar flares in the 2 - 8 keV energy range. The instrument was launched in August 1995 aboard the INTERBALL-Tail spacecraft. Description of the construction and operations is presented. The overall performance and the high sensitivity of the photometer is shown on examples. The X-ray tomograph-imager contains a unique rotationally modulated collimator. It provides sets of one-dimensional scans of flares taken at varying angles due to spinning of the satellite. We present principles of the algorithm for imaging from these data and show example of reconstructed flare image taken in the 2 - 4 keV range.

**Keywords:** solar physics; flares; X-ray photometry; X-ray imaging, instrumentation

## 1. Introduction

The Astronomical Institute of Czech Academy of Sciences has been involved in solar X-ray photometry since 1969. Early photometers have been placed on board a number of spacecraft including a series of Prognoz (5-10) elongated orbit probes. The most recent of these photometers is RF15-I (hereafter RF) instrument, which has been included as a part of the *INTERBALL-Tail* Mission. The instrument has been making measurements since August 6, 1995. As a partner in the RF experiment,

* email js@cbk.pan.wroc.pl

the Solar Physics Division of Polish Space Research Center became involved in the programme (in 1986), contributing to the unique X-ray Tomograph-Imager (XTI), a novel part of the instrument. Present circumstances allow the Polish Team to represent the PI for entire RF instrument and took over the responsibility for scientific output of the experiment. The present paper describes basic characteristics of the RF photometer, imager and presents examples of the data received. In a subsequent paper we will present details of data reduction and analysis. The photometer and XTI are physically and electronically separate. They are however controlled by a common onboard computer PRAM.

The *INTERBALL-Tail* is a spin-stabilized satellite placed on a highly elongated orbit, presently with ~182000 km apogee and ~24000 km perigee. The orbital period is ~96 hours. The satellite is directed from IKI (Russia) under the guidance of Prof. A. Galeev and Prof. L. Zelenyi. It operates within the STEP programme of multinational cooperation. Expected orbital life of the satellite extends till October 2000. The normal to the satellite instrument plate is pointed towards the solar centre within $\pm 10^\circ$ thanks to spin-stabilization of the spacecraft. One satellite revolution takes ~118 s. Every few days the satellite rotation axis is being repointed towards the solar centre as the Sun moves away at the rate of $\sim 1^\circ$/day due to Earth motion along the orbit.

## 2. General

The RF was developed in order to facilitate high-time resolution measurements of integral solar flux in the spectral energy range between 2 keV and 240 keV and to image solar flares in the bands 2 - 4 keV and 4 - 8 keV from rotationally modulated data (X-ray Tomograph-Imager, XTI). The photograph of RF instrument is shown in Fig. 1. The RF is equipped with five detector systems:

- Proportional gas-filled detector.
- NaI(Tl) scintillation detector with Al window.
- Three silicon detectors sensitive to charged particles (radiation belt detectors).
- Proportional detector behind the XTI.
- XTI attitude sensor (small optical refractor $\phi = 6\,\mathrm{mm}$).

Below we describe in more detail both instruments.

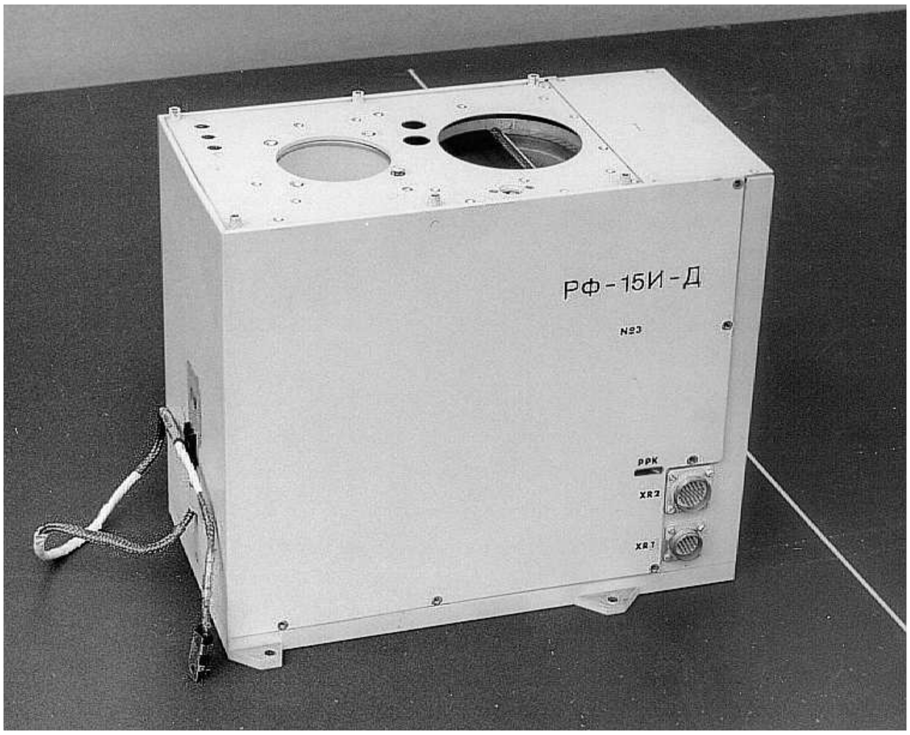


*Figure 1.* General appearance of the RF soft X-ray Photometer-Imager. The dimensions of the box shown are 300 ×155 × 254 mm. The box which contains both the photometer and the imager is placed atop the solar oriented platform of the spacecraft. RF is controlled using PRAM on-board computer placed inside the pressurized section of the satellite (not shown).

## 3. The Photometer

In Tables I - IV we present nominal energy ranges and essential characteristics of the proportional and scintillation detectors used in RF photometer. We split the presentations of detector's properties into

Table I. Nominal energy ranges and designations for the lower energy photometer channels (formatted into standard, common block of telemetry).

| Channel # | s1 | s2 * | s3 | h1 * |
|---|---|---|---|---|
| Energy band [keV] | $2-3$ | $3-5$ | $5-8$ | $10-15$ |
| Detector type | Prop. | Prop. | Prop. | Scint. |

*recorded in patrol/calibration mode

separate Tables (I and II) according to the way the data are formatted and put into the telemetry.

The proportional detectors consist of two cylindrical compartments with steel walls ~1.2 mm thick sharing the same gas. The section exposed to the solar radiation is equipped with the Be window in order to select the radiation with the energy above ~1 keV. The hidden (twin) section is illuminated by the radioactive calibration $Fe^{55}$ source. Corresponding calibration signal is constantly probed in order to detect ageing, leaking and other possible effects which may cause deterioration of the gas gain. Special electronic feedback system regulates accordingly the high voltage level on both anodes of the detector counteracting in this way the effects of gain variations. The energy discrimination thresholds are thus kept in place independent of the gain variations. However, towards the end of 1997, the activity of $Fe^{55}$ calibration source (7 years from fixing) decreased more than 10 times and went outside the limits of self-correction. Details of the gain time variations will be presented in a subsequent paper where the history of discrimination level positions will be given for entire duration of the mission. The average background count rate is ~10 cts/s for the proportional detector.

The scintillation detector contains 8 mm thick NaI(Tl) crystal with the Al filter ($0.25 \pm 0.01\, g/cm^2$ mass thickness) placed in front and a photomultiplier tube. This detector has its own calibration source ($Am^{241}$) but without feedback control.

In Figure 2, we present efficiencies of the proportional and scintillation detectors plotted against the photon energy. The incident solar photon flux is transmitted by detector window and absorbed by gas/crystal with the corresponding efficiencies. The redistribution over energies according to spectral response function takes place afterwards. The proportional detector collects soft X-ray photons in three energy bands 2 - 3 keV, 3 - 5 keV and 5 - 8 keV (see Table 1). The detector window is placed slightly below the instrument cover opening. This geometry causes the effective aperture to vary by few percent as the solar

Table II. Nominal energy ranges and designations for high-energy photometer channels recorded (in flare mode) into individual telemetry blocks. The measurements are reported every 125 msec.

| Channel # | h2 | h3 | h4 | h5 |
|---|---|---|---|---|
| Energy band [keV] | $15-30$ | $30-60$ | $60-120$ | $120-240$ |
| Detector type | Scint. | Scint. | Scint. | Scint. |

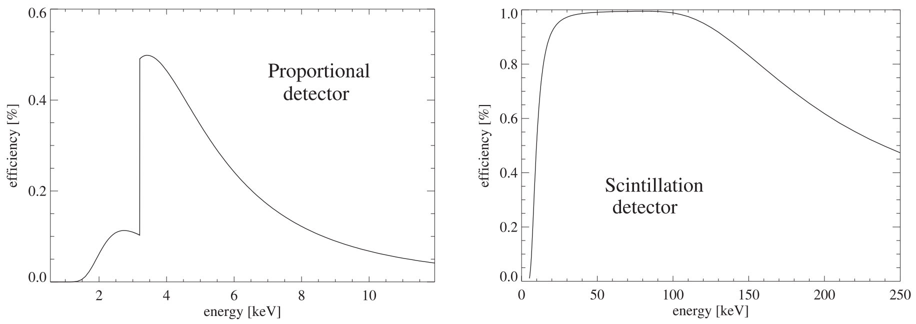


*Figure 2.* Spectral efficiency of the proportional (left) and scintillation (right) detectors as a function of photon energy.

illumination angle changes with the satellite spinning phase. Another factor contributing to modulation of the signal is that the absorption depth of the photon also depends on the rotation phase. This latter effect is especially important for higher energy radiation, for which the photon absorption length in the gas is greater than the detector depth.

The scintillation detector measures the hard X-ray flux in five energy bands (see Tables I and II). In flare mode the measurements are made every 0.125 s in the four highest energy channels. For these channels, the data are allowed to be transmitted to the telemetry provided that corresponding rate thresholds (40 cts/s) are exceeded for the four consecutive seconds. Otherwise, the data are not written in order to secure the telemetry volume. The channel h1 output is recorded differently. It is formatted together with the signal from the proportional detectors and sent to telemetry all the time (every 2 or 8 s) depending on the mode (flare or patrol). The adopted mode names may however be somewhat misleading, since the most of data have been collected in so-called flare mode. The reason for this was the selection of very low threshold for flare trigger. Actually it has been set at the level corresponding to microflare (few cts/s). Switching between patrol/flare modes is controlled onboard based on count rates recorded in s2 channel. Early in the mission, the instrument operated mostly in the flare mode, for periods up to several hours. Later on, following the change in the detector feedback control, the frequency of switching between the

Table III. Essential characteristics of the proportional detector.

| Aperture | Window | Gas Filling | Gas Depth | Energy resolution |
|---|---|---|---|---|
| 4.5 mm$^2$ | Be 150$\mu$m | Ar+10%$CO_2$, 350 Torr | 16 mm | 19% at 5.9 keV |

modes increased, and presently the photometer operates preferentially in patrol mode except for flares above *GOES* class B5 – B7.

During the patrol mode the calibration of the scintillation detector is made approximately every 2 hours (cf. Table I). For calibration, a moving arm equipped with $\mathrm{Am}^{241}$ radioactive source (half-decay time 432.2 years; energy 59.6 keV) is being mechanically inserted into the FOV of the detector. The calibration arm partly occults the aperture contributing to the signal in h1. In this way during the calibration the recorded signal responds in most cases to the calibration source quanta only. The other data reported at the time of calibration (s2 fluence) represent solar signal. The scintillation detector has no feedback control and therefore the ageing effects can be deduced only from analysis of time variations of the calibration level readouts. This analysis is in progress.

## 4. Examples of Photometer Observations

The RF instrument has been collecting data since August 6, 1995. Early during the mission, the measurements were made usually in the flare mode (i.e. in four channels, cf. Table I). Later on, the patrol mode measurements prevail. In Figs. 3 and 4, we show examples of data collected early during the mission. In Fig. 5 we compare the RF and *GOES* signals at appropriate channels. The comparison is presented for a period when the quiet solar X-ray signal has been at the very low level. Direct correspondence is observed which allows to relate the *GOES* flux to the appropriate RF flux and vice versa. The linear fit gives the following formula relating the two.

$$F_{GOES} = 2.98\,10^{-9} \times (F_{\mathrm{s1}} - 0.35) \qquad (1)$$

where $F_{GOES}$ is the flux in 1 - 8 Å band (in $W/m^2$) and $F_{\mathrm{s1}}$ is the count rate in s1 RF channel.

The analysis of data scatter indicates, that RF sensitivity is approximately equivalent to that of *GOES*. One of the noticeable deficiencies of RF photometry is the signal modulation due to spacecraft rotation.

Table IV. Essential characteristics of the scintillation detector.

| Aperture | Window | Crystal | Diameter/Thickness | Energy resolution |
|---|---|---|---|---|
| 1452 $\mathrm{mm}^2$ | Al $94 \pm 3\mu$ | NaI(Tl) | 43/8 mm | 22% at 59 keV |

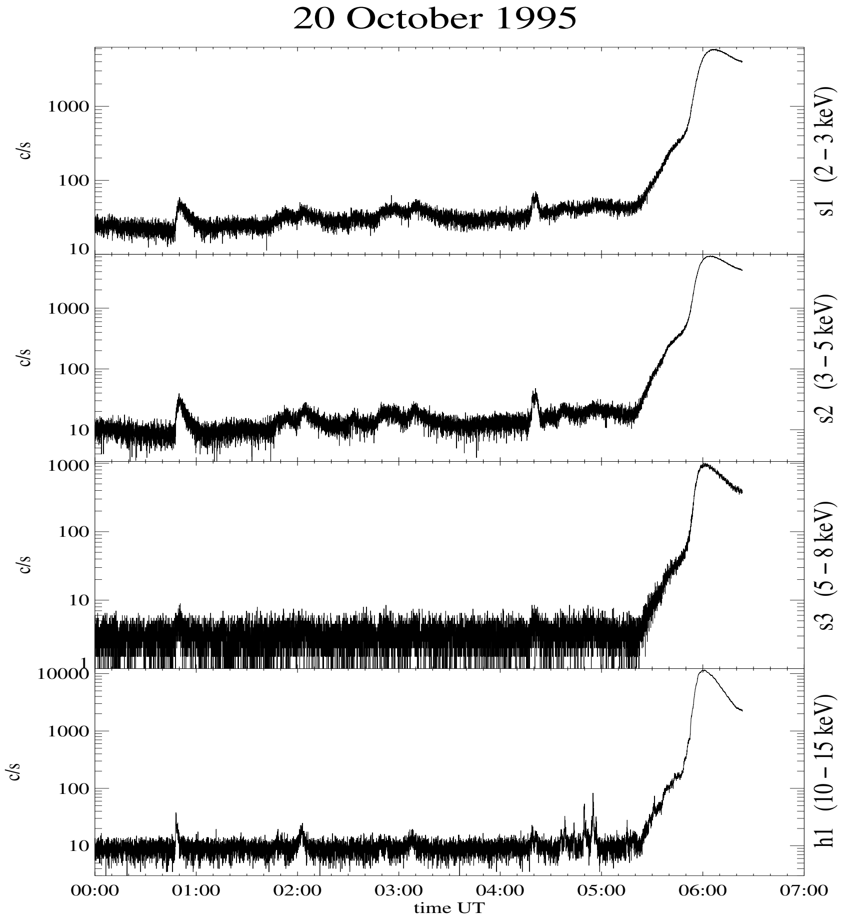


*Figure 3.* Time variability of solar X-ray emission as recorded in flare mode (every 2 s) in four lower energy channels: s1, s2, s3 and h1 for a selected time interval on 20 October 1995. The measurements cover 7 hours of uninterrupted observations. The smallest/largest enhancements seen correspond (in *GOES* X-ray classification) to B1.3 and M1.5 flares respectively. In channels s1, s2 and h1, the basal level contains valid solar signal. In channel s3, the basal level represents the detector background only.

These observed modulations have few percent relative amplitudes and the period around 118 s. In order to remove the fluctuations, we have determined appropriate phase modulation profiles (for each of the channels separately) using epoch folding (details of the procedure will be described in a subsequent paper). These folded profiles have been next used in order to remove the modulation from the raw data. At present, we are in the process of systematic reformatting and regularizing the data. At our web site

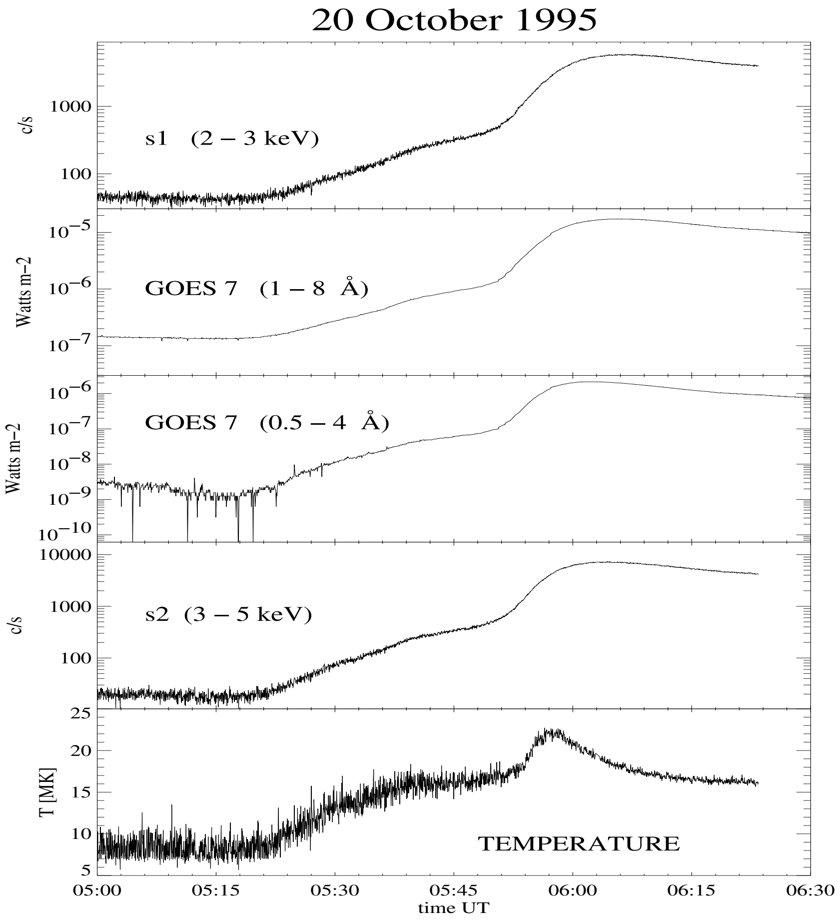


*Figure 4.* A portion of Figure 3 showing the light curves for the 20 October 1995 M1.5 flare in more details. RF light curves are plotted in the upper and the fourth panels. Corresponding *GOES* lightcurves are presented in between for comparison. The observed variations in the (s2/s1) flux ratio have been interpreted in terms of an average source plasma temperature. Resulting temperature variation plot is presented in the lowest panel.

(`www.cbk.pan.wroc.pl/rf15-i_www/RF15-I _observations.htm`) we put all the data processed so far along with short explanations. On a positive side is that the modulation of the signal due to the satellite rotation allows for distinguishing between solar X-ray emission and non- solar particle contribution (the last being usually not modulated).

One of the important advantages of RF measurements is that there are many periods where the solar signal has been measured every 2 s continuously for up to 40 hours in the four energy bands.

The overall data coverage of the solar X-ray photometry is $\sim 85\%$.

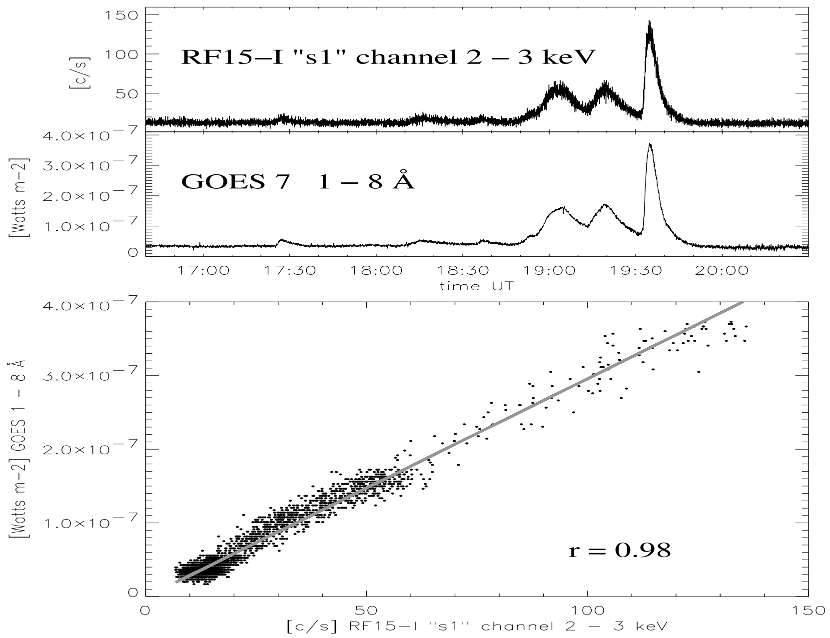


*Figure 5.* Comparison of RF and *GOES* records for corresponding energy bands of both instruments. Few weak flares have been observed on 8 August 1995, within the period selected for the comparison. This is illustrated in the upper panel where the light curves are plotted. In the bottom panel the corresponding correlation diagram is presented with the value of correlation coefficient $r$ given.

The physical analysis of data is in progress. In the example shown in Figure 4 (bottom panel) we present derived variations of coronal source plasma temperature as determined in the isothermal approximation from the ratio of fluxes recorded in the s1 and s2 bands. One may notice that the scatter in derived temperature is relatively small and that the temperatures are within realistic range also for periods where no flare in progress has been reported. Details of the physical data analysis will be published in a forthcoming paper.

As concerns the data collected in the higher energy channels, reliable measurements have been made for hundreds of events (Siarkowski *et al.*, 1999). Analysis of this data indicates that during strong events, pile-up effects might contribute to the flux in higher energy channels, as well as the detector dead time effects may become important (as pointed up by the Referee). The dead-time for electronics of both proportional and scintillation counters is 8$\mu$s, larger than intrinsic detector's physical dead-times. Therefore, the effects of pile-up and dead-time corrections

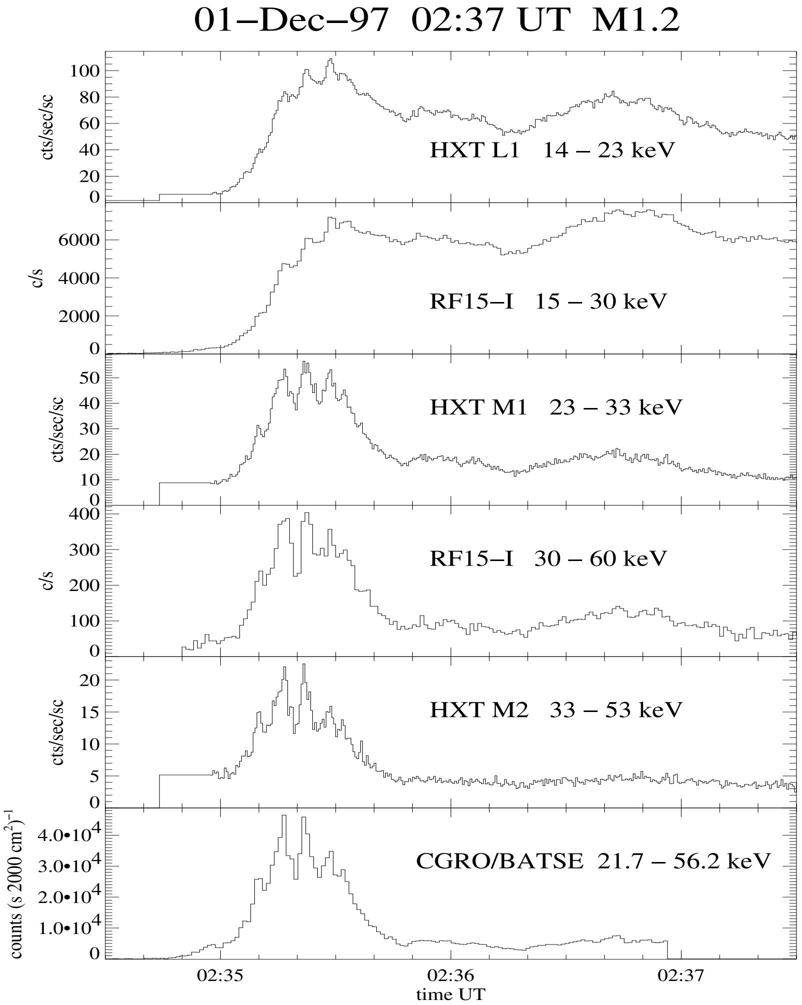


*Figure 6.* Comparison of higher energy RF records with corresponding *Yohkoh* HXT and *BATSE* (bottom) light curves for the 1 December 1997 flare. The rates observed in RF channels shown are not corrected for the pile-up and dead-time effects which may lower by up to 20% the rates observed around flare maximum.

will become important (at 10% level) for count rates above $10^4$ cts/s. A more detailed consideration of these problems will be given in the forthcoming paper.

For the M1.2 flare shown in Fig. 6, RF recorded the fluxes in h2 and h3 energy channels. This flare has been observed also by *Yohkoh* HXT and *BATSE*. We put corresponding lightcurves in the Figure for the comparison. The overall agreement of signals in corresponding energy bands is very good (for description of the HXT construction see Kosugi et. al., 1991). Detailed cross-calibration between RF, *GOES*, HXT and *BATSE* measurements is in progress.

The higher energy RF data are also presented and available from our web server.

While crossing van Allen radiation belts the detectors were designed to be switched-off. We noticed however that on several occasions the particle flux has been low enough not to trigger the in-belt flag. Therefore the detectors did not switch-off and recorded signal due to particles. This resulted in a characteristic pattern of recordings in all channels of RF. Such particle events can be easily recognized through their specific inverted/flat energy spectrum. On at least one occasion the non-solar hard X-ray event has been detected, originating from the SRG1900+14 burst (Sylwester *et al.*, 1998).

We have encountered a number of problems during data reduction and prompt analysis. For example, the count rate level from large flares (i.e. above M5-M6 *GOES* class) exceeds the capacity of counters (set at 32000 and 64000 hits per integration time in particular channels). This caused counter wrapping, sometimes many-fold.

## 5. The X-ray Tomograph-Imager

A concept of imaging modulation collimator is based on reconstruction of full two-dimensional images from sets of one-dimensional projections. The principles of the (rotating) modulation collimator have been described in-depth by Oda *et al.* (1976) and Tsuneta (1984). Progress in technology and three-axis attitude stabilization of satellites resulted in development of the fixed imaging collimators (HXIS; van Beek, 1976) and telescopes with the CCD devices (*Yohkoh* SXT). However, high-energy (above 10 keV) images can be obtained by making use of modulation collimator technique alone (e.g., *Yohkoh* HXT), in which a concept rotating modulation collimator aboard a spin- axis stabilized spacecraft may be the simplest form of instrument hardware. Presently, the HESSI instument (under development, Lin *et al.* 1998) also incorporates this concept. One of the best examples of the results obtained using rotationally modulated collimators are the hard X-ray images of solar flares from the Japanese satellite *HINOTORI* (Tsuneta, 1984).

In disigning the X-ray Tomograph-Imager we incorporated a similar, but modified concept of the construction of the rotationally modulated collimator. In the following we present a description of this instument called X-ray Tomograph-Imager (XTI), principles of its operation and a brief information on the image reconstruction algorithm. More in-depth description of this imager will be given in a separate paper.

The XTI consists of two units:

– The X-ray collimator, and
– The optical solar disk sensor.

The construction of the units is described below.

### 5.1. The X-ray Collimator (XRC)

The purpose of XRC is to modulate and measure the X-ray signal from flares and the hottest part of active regions. Since the rotation axis of the *INTERBALL-Tail* satellite is mostly offset from the X-ray source by a few degrees, the recurrent transmission windows of the collimator become available for modulation of X-rays, as the phase of source relative to the optical plane of the collimator changes. The concept of the collimator construction adopted in XTI is presented in Figure 7. The essential construction characteristics of the collimator are illustrated in Fig. 8 and given in Table V. The XRC consists of a system of three precisely co-aligned grid planes placed in front of the double proportional counter operating in the 2 - 4 keV and 4 - 8 keV energy ranges. The detector is analogous to that used in the photometer, but there are different electronics and discrimination thresholds. The feedback control is used to counteract the gain variations, as described earlier.

Due to rotation of the satellite, the X-rays from a solar source are modulated, depending on the actual phase of the rotation. The collimator field of view has a radius of $\sim 11^{\circ}$, and the collimator has been designed to have a number of narrow transmission windows separated by 4.8 arc min. These selected design characteristics allow to isolate a flaring area in the Sun covering thus the entire flare without overlapping (provided it has extension smaller than $4.8 \times 4.8$ arc min). In order to have a simpler pattern of modulation fringes, we decided to make grids of circular cross-section wires. A cheap and easy solution was to use standard copper wires. Copper has enough atomic mass to block the harder part of the radiation if of sufficient radius. We selected to use wires of $66.8\,\mu$m diameter on the front and bottom grids and $50.0\,\mu$m for the middle grid. The wire orientation has been fixed exactly parallel (to within $\pm 1\mu$m) between the three grid planes using an interferometric technique. The main characteristics of the collimator are given in Table V and in Fig. 8. The grid plane positions, exact wire diameters and the pitch have been designed according to the physical requirements. The collimator construction allows for slight manufacture errors (8 $\mu$m) in placing grids within particular grid plane, without affecting the desired transmission pattern of the entire collimator.

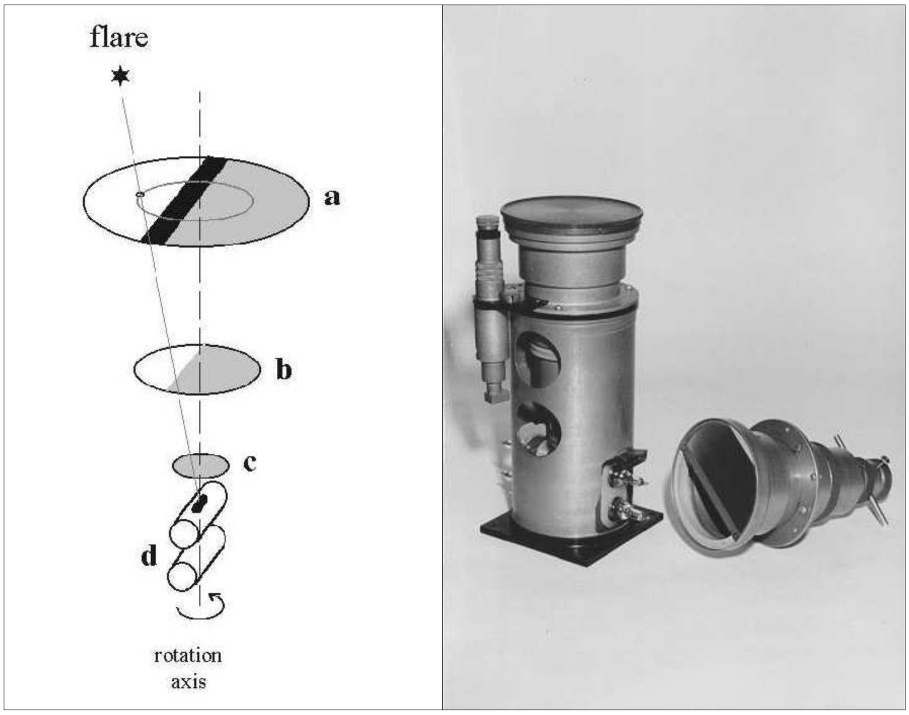


*Figure 7.* The principle of the operation (left) and the photo of the X-ray collimator unit. The solar flare X-rays are illuminating the double proportional detector (**d**) through a system of three grids. The front grid (**a**) contains three regions i.e.: partly open area, occulting bar, and gridded area (shaded). The middle grid (**b**) is half open and the bottom one is completely filled with grids. The grids are made of the copper wires precisely coaligned. The bottom grid is located immediately in front of the double proportional counter detector (**d**) with a window of $3\times 10$ mm size. In the photo (right) the entire collimator unit is presented (assembled and disassembled). The optical disk sensor is attached outside, parallel to the collimator axis.

Table V. Essential characteristics of the Collimator (see Fig. 8)

| Length | Fringe separation | FWHM | Transmission* in X-rays | Energy bands | Readout rate |
|---|---|---|---|---|---|
| 160 mm | 4.8 arc min | 11 arc sec | 0.08 | 2 - 4 keV | 1/128 s |
| | | | 0.09 | 4 - 8 keV | 1/128 s |

*ratio of transmitted to illuminating fluxes; diffraction effects have been taken into account

The exact location of the grid planes have been calculated according to a novel strategy. The novelty of the solution is the use of semi-numerical interactive method of placing the grids. In case of the XTI, we specified the approximate values for the collimator length, thickness of grids, desired resolution and transmission fringe separation and found the optimum collimator design as presented in Fig. 8. The collimator grid system has been co-aligned by visible light technique with diffraction effects taken into account. We measured separately the transmission in X-rays. The area averaged rms alignment accuracy has been found to be $\pm 1\,\mu$m, and the maximum wire misalignment found is $\sim 10\,\mu$m.

As shown in Fig. 8, the front and the middle grid wired sections cover only a portion (approximately half) of the planes. The front grid has additionally an occultation strip. The width of this strip is selected to be 6.2 mm allowing thus to ensure that the solar disk will be fully eclipsed (as seen from the detector window). With the Sun crossing the bar, the solar X-rays are totally blocked permitting measurements of the background signal (cf. Fig. 8).

In Fig. 9 we schematically draw the trajectory of a compact solar source (flare) as seen in the coordinate system of the collimator (front grid). Provided nutation is negligible, the solar source trajectory is a circular path crossing the open area, occultation bar and gridded area. Depending on the offset $\delta$ of the source relative to the axis of the collimator, a number of modulation patterns are expected:

- no bar occultation for $\delta < 0.54°$
- single partial bar occultation for $0.54° < \delta < 1.55°$
- double partial bar occultation for $1.55° < \delta < 2.63°$
- full modulation pattern (as in Fig. 9) for $\delta > 3.64°$

An example of calculated characteristic pattern of the signal modulation is shown in Figure 10.

The actual position of the satellite rotation axis relative to the optical solar disk is monitored by a dedicated optical sensor unit described below.

### 5.2. The Optical Solar disk Sensor (SDS)

The optical solar disk sensor (SDS) was intended to be used in order to establish distance between disk center and the X-ray source. This would enable for potential identification of the active region contributing to the X-ray signal. By incorporating the satellite attitude data, it would be possible to determine the rotation phase relative to the celestial coordinate system, fixing thus the absolute source position on the disk.

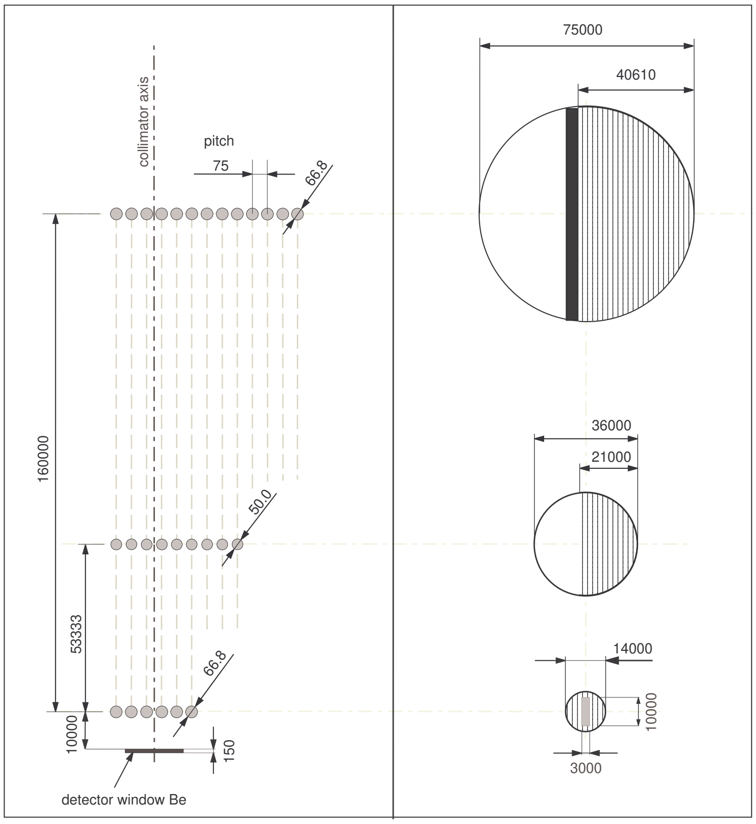


*Figure 8.* Details of mechanical construction of the collimator as seen from the side along the the wires (left) and from the top (three right circles). All dimensions are given in $\mu$m. The wires are of circular cross- section with diameters $\phi = 66.8\,\mu$m for front and bottom grids and $\phi = 50.0\,\mu$m for the middle grid. Pitch is $75.0\,\mu$m in each grid plane. The diagram is drawn not to scale. In the right panel, the three grid planes are depicted as seen from the front. Preserved are the proportions between the grid sizes and gridded/occulted/open areas. The position of the detector window aperture ($3 \times 10$ mm) is projected on the lower, fully wired grid.

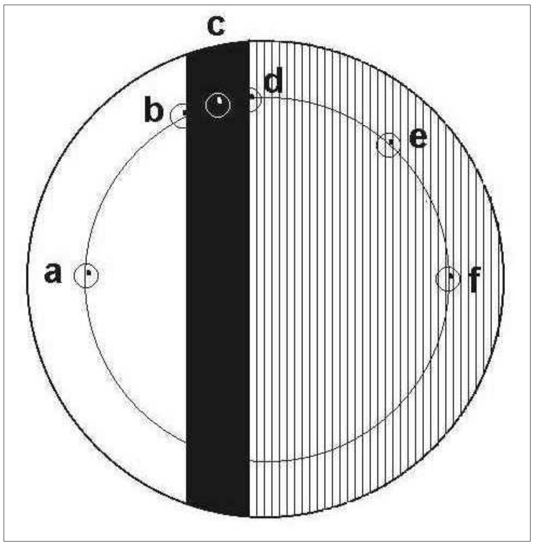


*Figure 9.* A scheme showing various phases of the modulation of the solar radiation passing through the collimator. The Sun is shown as a small circle with the X-ray source as a small spot placed inside. Due to rotation of the spacecraft the apparent position of the source, as seen from the detector window, follows the circular path. For a part of the rotation period (phase **a**) no modulation of the signal is observed. At phase **b** the source enters the occultation strip which angular width is more than the solar diameter and therefore, at phase **c**, the solar soft X-ray radiation is totally blocked. In this period the signal recorded corresponds to the detector background. At phase **d** the source enters the gridded section of the collimator and the signal is frequently modulated when the source crosses individual transmission windows. At each transmission window, the X-ray source is scanned at different angle (changing by $\pi/2$ between phases **d** and **f**).

The SDS unit consists of the optical system which projects images of the solar disk on the system of two narrow slits. The optical axis of SDS is coaligned with the axis of the X-ray collimator. The slits are adjusted to be parallel to the occulting bar. Spinning of the spacecraft causes the projected optical solar disk to circle through the double slit system presented in Fig. 11.

Behind the slit system, the photodiode monitors the overall optical flux passing through the slit system. A dedicated on-board computer routine analyzes the slit crossing times and determines corresponding phases of rotation and the solar centre offset angle based on the history of slit crossing times from the previous rotation. The slit crossing times were envisaged to be dumped to the telemetry after every 100 satellite rotations.

It is by misfortune that during the pre-flight preparations immediately preceding the launch from the Baikonur, the aperture of the SDS

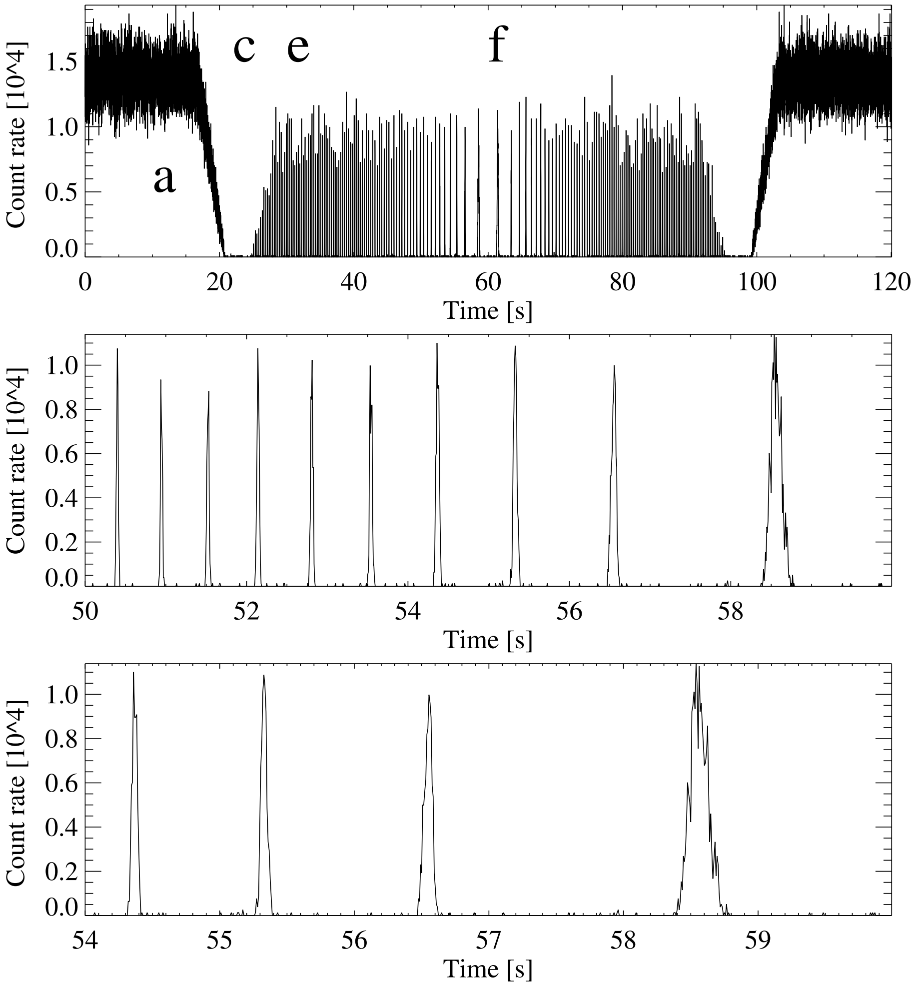


*Figure 10.* Numerically simulated noisy pattern of the X-ray signal modulation. The individual phases of the depicted pattern correspond directly to the passage of the X-ray source through individual sections of the collimator (as indicated in Figure 9). The number of peaks in the modulated pattern depends on the angular distance $\delta$ of the source relative to the satellite spin axis. The profiles within individual fringes depend on the distribution of X-ray brightness within the localized emitting region.

optical sensor has not been cleared. As a consequence we are missing the data from this sensor. We have fortunately foresighted for such an unfortunate situation and pre-programmed a safe-mode activity for the XTI in such circumstances.

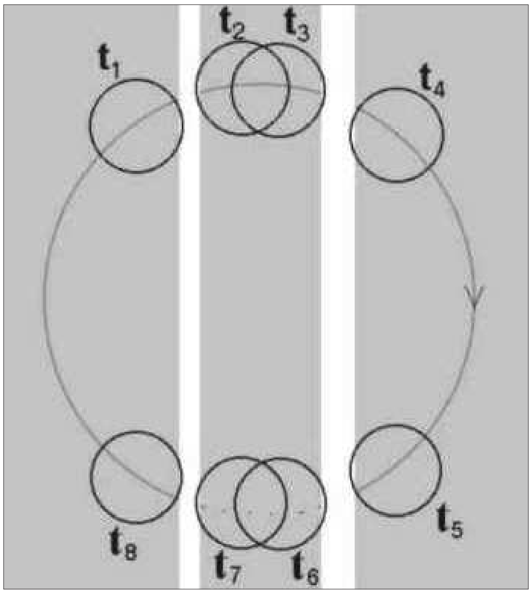


*Figure 11.* Scheme of the motion of the visible image of the solar disk across the system of the slits in the SDS unit. At crossing times $t_1$ - $t_8$ the electronic system connected to the photodiode located behind the grids issues flags informing that the solar disk enters/leaves individual slits. Since the apparent angular width of one of the slits is twice the other, the on-board computer is able to recognize the direction of the motion and calculate the instant phase of the rotation from the slit crossing timing. The scheme is made up to show apparent angular scales as concerns slit widths and solar diameter.

### 5.3. On-board data processing

The signals incoming from the XTI are being processed in real time by the PRAM onboard computer and stored temporarily to the onboard memory before being sent to the ground.

In order to effectively use the memory capacity, we devised an elaborated scheme of on-board signal processing, which saves the memory and allows to concentrate on flare events occuring between consecutive telemetry dumps. In particular, the signal from XTI X-ray detector is constantly monitored in order to detect the flare occurence. Flare intensity class is being estimated in real time and the decision is made on-board when and which observing sequence is to be executed. Even with such elaborated scheme, only $\sim 80$ compressed image modulation sequences can be stored in the on-board memory between consecutive ground telemetry dumps (say one sequence per hour on average).

The following XTI operation modes have been preprogrammed:

– low activity – only minimum and maximum X-ray rate values for a given S/C spin are stored;

- high activity – detailed modulated signal together with extreme and averaged values of the background from unmodulated signal are preserved. Interfringe zeros are discarded.

Such organization of the data collection compresses substantially the volume of the data to be recorded on-board, but necessarily needs the time stamp from the onboard clock to be assigned to each data package. In order to shorten the time info byte length, the local clock has been used giving only the data pack number in a sequence.

The telemetry storage threshold flag level is being determined on-board by comparing the X-ray signal with the dynamically changing remaining telemetry quota. This telemetry quota depends on a recent history of solar flare activity. If no flares have been observed towards the time of the following telemetry dump, the modulation patterns are forced to be recorded independent of the solar activity level, in order to fill the telemetry allocated. If a flare is being detected, the program seeks for the period of flare maximum to occur. When found, the modulation sequence is stored. Around the flare maximum phase, when the time variability of the signal is small, we expect the morphological changes in the flare structure to be slow enough to allow (ideally) for realistic image reconstruction from the data taken within a half of the modulated portion of the rotation lasting $\sim 30$ s).

### 5.4. Example Observations from XTI

In Figure 12, an example of the XTI modulated signal for the 20 October 1995 flare is shown. There are hundreds of periods identified already where the imaging sequences have been executed. We will present detailed analysis of these periods in one of a subsequent publications.

### 5.5. Deconvolution of XTI images

The solar X-ray source (flare) is scanned at various angles (directions) due to spinning motion of the satellite. The detector signal in any of the transmission fringes represents one-dimensional projection of the two-dimensional source brightness distribution. As the phase of the rotation changes views from many projection angles are recorded. A resulting set of multiple one-dimensional scans constitutes the input for the numerical image reconstruction algorithm. Below, we briefly introduce the basics of this image reconstruction algorithm.

In Fig. 13 we present definitions used when formulating the problem of image reconstruction. In this representation $f(k,l)$ is the X-ray brightness of the investigated source. Fixed coordinate system $(k,l)$ is

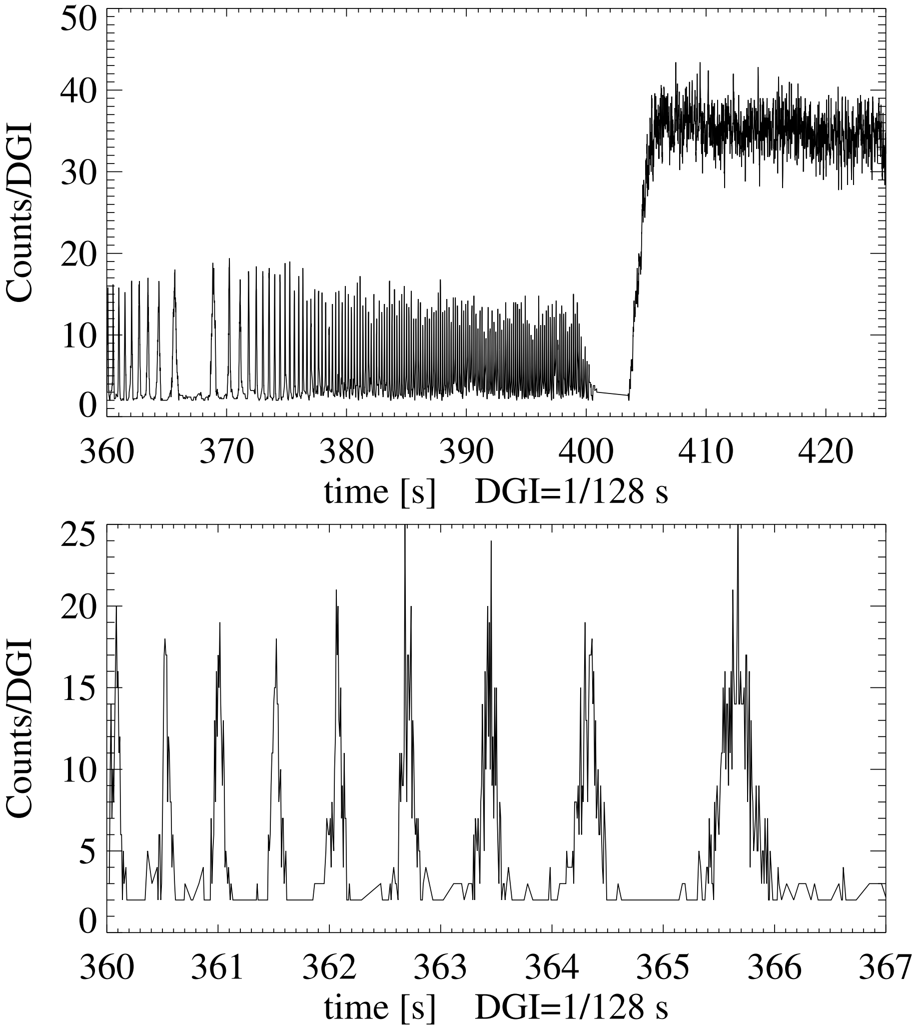


*Figure 12.* The observed modulation of the X-ray signal in the 2 - 4 keV band of the X-ray Tomograph-Imager (XTI) for 20 October 1995 flare. In the bottom panel, initial small portion of the recorded signal is enlarged in order to present more details of the record shown above. On the horizontal axis the time elapsed from the start of this particular modulation sequence is indicated.

used. During the scan, the value of the measured signal in each position (time bin represented as column $m$ perpendicular to the scan direction) represents a result of convolution of the collimator transmission function $g$ and the source intensity integrated along this perpendicular direction. Thus, the flux measured in bin number $j$ can be expressed

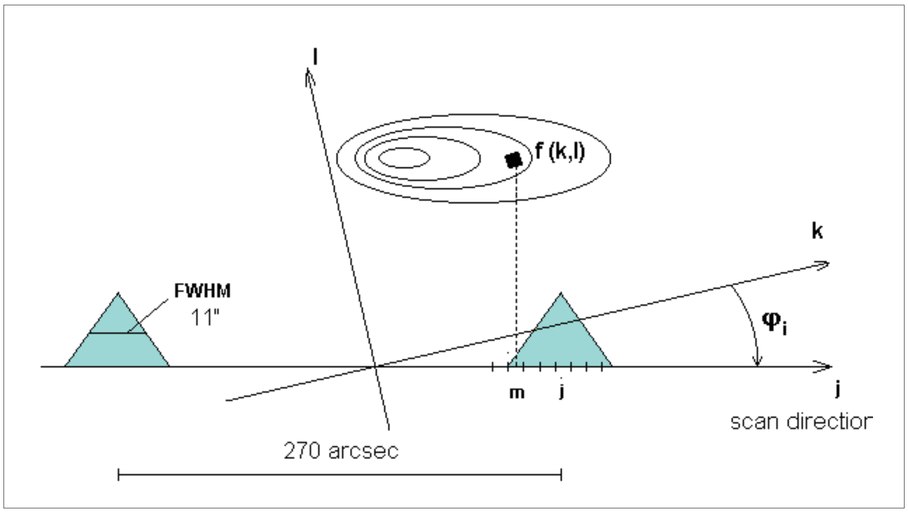


*Figure 13.* Basic formulation of image reconstruction problem. See the text for details.

as:

$$I(j) = \sum_{m} f(m) g(j - m) \qquad (2)$$

For the purpose of image reconstruction we have assumed the collimator transmission function to consist of a number of triangular profiles (windows) with FWHM $= b = 11$ arcsec. The consecutive transmission windows are separated by the angular distance $p = 288$ arcsec. In the assumed coordinate system, the transmission $g$ in bin $j$ is:

$$g(j) = \begin{cases} 1 - \frac{|jd - np|}{b} & , \text{ when } |jd - np| \leq b \\ 0 & , \text{ when } |jd - np| > b \end{cases} \qquad (3)$$

where $d$ is the bin width and $n = 0, 1, 2, \ldots$ is the index of particular transmission window. In case of scan taken at the position angle $\varphi_i$, the value of $m$ in Eq. (2) is $k\ cos\ \varphi_i + l\ sin\ \varphi_i$, so the signal measured in bin $j$ can be expressed as:

$$I(j,\ \varphi_i) = \sum_{k,l} f(k,\ l)\, g(j - k\ cos\ \varphi_i - l\ sin\ \varphi_i) \qquad (4)$$

For compact sources with spatial extension smaller than the separation between transmission fringes, only a single transmission FOV contributes to the signal. By rotating the collimator relative to the source, its brightness distribution $f_{kl}$ is recorded in a set of intensity vectors $I_{ij}$ (corresponding to individual scans). This transformation is handled by a transmission tensor $g_{ijkl}$.

$$I_{ij} = \sum_{k,l} f_{kl}\, g_{ijkl} \tag{5}$$

The purpose of image restoration process is to solve the inverse problem i.e. to determine $f(k,l)$ from measured $I_{ij}$. We have developed an elaborated maximum likelihood iterative procedure to solve this inverse problem. Within the algorithm, we assume a uniform brightness distribution as an initial approximation ($f_{kl} = const$). The subsequent (improved, $n+1$) approximation for $f_{kl}^{n+1}$ distribution is obtained by multiplying the preceding result by the appropriate correction matrix. This correction matrix represents the ratio of the observed ($O$) and calculated ($C$) flux in each bin, weighted by the collimator transmission function:

$$f_{kl}^{n+1} = f_{kl}^{n} \frac{\sum\limits_{i,j} \frac{I_{ij}^{O}}{I_{ij}^{C}}\, g_{ijkl}}{\sum\limits_{i,j} g_{ijkl}} \ . \tag{6}$$

For instance, if the observed flux at bin $j$ is greater the calculated one, we increase the brightness in each of the pixels $(k,l)$ which contribute to this bin (in proportion to the corresponding individual weights of the collimator transmission function).

The quality of the iterative convergence is judged in terms of $\chi^2$ statistics. The process of image reconstruction is terminated when the value of reduced $\chi^2$ approaches unity.

The inversion technique used here is a straightforward extension of one- and two-dimensional maximum likelihood iterative inversion methods commonly used for solar X-ray data analysis (Sylwester, Schrijver and Mewe, 1980; Svestka *et al.*, 1983, Sylwester and Sylwester, 1998, 1999). It is analogous of the computer tomography image reconstruction procedure used in medical applications, where scans from many directions are used to generate two–dimensional picture of (slices) of the body internal structure.

The method used is inherently positively constrained since it uses multiplicative corrections based on observed to calculated (weighted) flux ratios. Within the present method it is possible to vary the pixel size in the reconstructed image, independently of the size or the number of modulation scans used for image reconstruction. At present, we perform deconvolution using 10 arcsec $\times 10$ arcsec pixel size in the deconvolved image. We will look for the solutions with finer mesh in the future. In Fig. 14 we present an example of the reconstructed image for the 20 October 1995 flare observed around 06:14 UT. The lightcurves

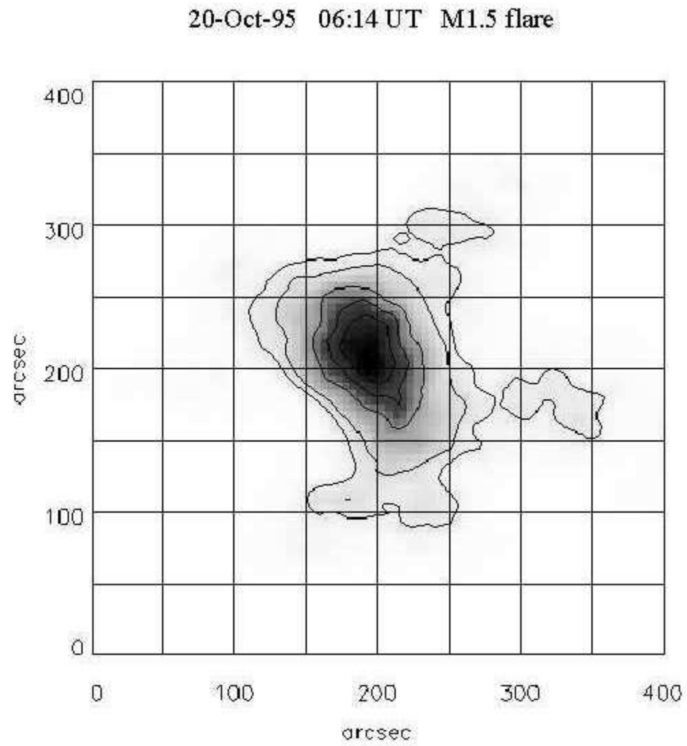


*Figure 14.* Example of reconstructed flare image (at 06:14 UT), close to the maximum phase of 20 October 1995 M1.5 flare. The event took place on a disk, close to the South-West solar limb.

of this flare are shown in Fig. 4. The flare took place on the disk (S09 W55). The limiting spatial resolution on the reconstructed image depends on many factors such as the signal/noise ratio of the modulated signal, the amplitude of nutation of the spacecraft rotation axis and the time variations of brightness within the flaring structure during the modulation period (we assume the latter not to change during this time). There are hundreds of identified modulation sequencies available for the image reconstruction. We will perform their analysis in the near future.

## 6. Conclusions

We present the RF15-I soft/hard X-ray photometer/imager presently aboard the *INTERBALL-Tail* Probe. The RF appears to be one of the most sensitive solar photometers in the 10 - 15 keV band and the only X-ray instrument measuring presently integral solar flux in the entire energy range 2 - 240 keV. By observing the Sun since September 1995 this photometer has supplied complementary data to *GOES*, *BATSE* and HXT *Yohkoh* measurements. In particular till the end of 1997, 150 flares have been observed for which H$\alpha$ observations have been reported and no *GOES* class have been assigned. Many flares have been detected with the hard X-ray emission extending up to 30 keV - 60 keV which have fallen into times of the *BATSE* and/or *Yohkoh* nights and hence have not been reported by those Teams. A number of weak (*GOES* class B) flare events have been observed to pronounce exceptionally hard X-ray spectra extending up to $\sim$120 keV energy (Siarkowski *et al.*, 1999). Collected data constitute a viable source for investigations of X-ray solar global oscillations, flare energetics and weak events statistics. Future data analysis will hopefully reveal more details on the coronal and flare heating and particle acceleration processes. We envisage that the data can also be usefull in studies of processes responsible for formation of magnetospheric X-rays within the auroral regions, since there are indications that such an emission has also been observed by the RF detectors.

The X-ray tomograph-imager, a unique rotationally modulated collimator, provides sets of one-dimensional scans of flares taken at varying angles. We present principles of the algorithm of the numerical analysis of these data used to reconstruct images of solar flares in the range 2 - 4 - 8 keV. Comparison of these reconstructed images with those obtained from *Yohkoh* HXT advanced imager is in progress. The results of such comparison will possibly allow to develop next generation rotationally modulated hard X-ray imagers.

## 7. Acknowledgements

The construction of RF has been possible thanks to enthusiasm of many people including Jiri Ullrich and Miroslav Halik from Czech Republic, and J. Bąkała, E. Stańczyk and R. Zawerbny from Poland. We would especially thank J. Bąkała and S. Gburek for preparing some figures included in this paper. In the present contribution we have presented data obtained through the CGRO *BATSE* Solar Flare Data Archive maintained by the Solar Data Analysis Center at NASA-Goddard Space Flight Center and provided by the *BATSE* team headed by Dr. G. Fishman. *GOES* X-ray data have been taken from SEC NOAA. *Yohkoh* HXT data have been analysed using the software developed by the Japanese Team.

Our final special thanks are to the Referee of this paper, Professor Takeo Kosugi (PI for HXT) for his kind critical comments and corrections which definitely lead to the improvement of this paper content, organisation and presentation.

This contribution has been supported by grant 2.P03C.006.13 of Polish State Committee for Scientific Research (KBN).

## References

van Beek H.F.: 1976, *Space Science Instrumentation*, **2**, 197.

Kosugi T., Mikishima K., Murakami T., Sakao T., Dotani T., Inda M., Kai K., Masuda S., Nakajima H., Ogawara Y., Sawa M., and Shibasaki K.: 1991, *Solar Phys.*, **136**, 17.

Lin R.P. *at al.*: 1998, 'High-Energy Solar Spectroscopic Imager (HESSI) Small Explorer Mission for the Next (2000) Solar Maximum', in C. M. Korendyke (ed.) *'Missions to the Sun II'*, Proc. SPIE Vol. 3442, p. 2

Oda M. Muranaka N., Matsuoka M., Miyamoto S., and Ogawara Y.: 1976, *Space Science Instrumentation*, **2**, 141.

Siarkowski M., Sylwester J., Gburek S., and Kordylewski Z.: 1999, 'Review of RF15-I X-ray Photometer Observations', in A. Wilson (ed.) *Magnetic Fields and Solar Processes*, ESA, SP-448, p. 877.

Svestka Z., Schrijver J., Somov B.R., Dennis B.E., Woodgate B.E., Furst E., Hirth W., Klein L., and Raoult A.: 1983, *Solar Phys.*, **85**, 313.

Sylwester J., Kordylewski Z., Siarkowski S., Gburek S., Farnik F., and Likin O.:1998, *Acta Astronomica*, **48**, 819.

Sylwester J., Schrijver J., Mewe R.: 1980, *Solar Phys.*, **67**, 285.

Sylwester J. and Sylwester B.:1998, *Acta Astronomica*, **48**, 519.

Sylwester J. and Sylwester B.:1999, *Acta Astronomica*, **49**, 189.

Tsuneta S.: 1984, *Ann Tokyo Astron. Obs.*, **20**, 1.